

Mathematical Modeling of Intraplaque Neovascularization and Hemorrhage in a Carotid Atherosclerotic Plaque

Y Cai (✉ yancai@seu.edu.cn)

Southeast University

Jichao Pan

Southeast University

Zhiyong Li

Southeast University

Research

Keywords: Mathematical modeling of vulnerable plaque, Intraplaque neovascularization and hemorrhage, Dynamics of plaque microenvironmental factors

Posted Date: March 13th, 2021

DOI: <https://doi.org/10.21203/rs.3.rs-291459/v1>

License:  This work is licensed under a Creative Commons Attribution 4.0 International License.

[Read Full License](#)

Mathematical modeling of intraplaque neovascularization and hemorrhage in a carotid atherosclerotic plaque

Yan Cai^{1,*}, Jichao Pan¹ and Zhiyong Li^{1,2}

¹ School of Biological Sciences & Medical Engineering, Southeast University, Nanjing, China

² School of Mechanical, Medical and Process Engineering, Queensland University of Technology, Brisbane, QLD 4001, Australia

*Corresponding Author: Yan Cai. Email: yancai@seu.edu.cn

Abstract: Background Growing experimental evidence has identified neovascularization from the adventitial vasa vasorum and induced intraplaque hemorrhage (IPH) as critical indicators during the development of vulnerable atherosclerotic plaques. In this study, we propose a mathematical model incorporating intraplaque angiogenesis and hemodynamic calculation of the microcirculation, in order to obtain the quantitative evaluation of the influences of intraplaque neovascularization and hemorrhage on the vulnerable plaque development. A two-dimensional nine-point model of angiogenic microvasculature is generated based on histology of a patient's carotid plaque. The intraplaque angiogenesis model includes three key cells (endothelial cells, smooth muscle cells and macrophages) and three key chemical factors (vascular endothelial growth factors, extracellular matrix and matrix metalloproteinase), which densities and concentrations are described by a series of reaction-diffusion equations. The hemodynamic calculation by coupling the intravascular blood flow, the extravascular plasma flow and the transvascular transport is carried out on the generated angiogenic microvessel network. We then define the IPH area by using the plasma concentration in the interstitial tissue, as well as the extravascular transport across the capillary wall. **Results** The simulational results reproduce a series of pathophysiological phenomena during the atherosclerotic plaque progression, such as the high microvessel density region at the shoulder areas, the enlarged necrotic core, and the IPH caused by the extravascular plasma flow across the leaky wall of the neovasculature. The simulational results show significant consistency with both the MR imaging data and in vitro experimental observations in quantity ground. Moreover, the sensitivity analysis of model parameters reveals that the IPH area and extent can be reduced significantly by decreasing the MVD and the wall permeability of the neovasculature. **Conclusions** The current

quantitative model could help us to better understand the roles of microvascular and intraplaque hemorrhage during the carotid plaque progression.

Keywords: Mathematical modeling of vulnerable plaque; Intraplaque neovascularization and hemorrhage; Dynamics of plaque microenvironmental factors

1. Background

Atherosclerosis is the process in which plaques, consisting of lipoproteins, monocyte/macrophages, vascular smooth muscle cells (SMCs) and platelets, are built up in the injured walls of arteries as a chronic inflammatory response. In the early phase of the plaque development, hypercholesterolemia conditions increase low density lipoprotein (LDL) infiltration and retention into the injured endothelial layer in response to disturbed blood flow pattern, leading to the accumulation of inflammatory cells by the release of pro-inflammatory factors, such as monocyte chemoattractant protein (MCP-1). Meanwhile, vascular SMCs undergo phenotypic dedifferentiation that from quiescent phenotype to a synthetic and activated phenotype, in response to pro-inflammatory cytokines and oxidized LDL (ox-LDL). As the atherosclerotic plaque develops, a hypoxic microenvironment in the plaque lesion is forming due to the increased oxygen consumption caused by high metabolic active cells (such as macrophages). This pathological microenvironment will trigger intraplaque neovascularization by upregulation of pro-angiogenic factors, such as vascular endothelial growth factors (VEGFs). The angiogenic microvessels generated from the adventitial vasa vasorum transport blood-borne components including inflammatory cells and lipoproteins into the lesion, which can exacerbate the lipid and inflammatory microenvironment inside the plaques [1,2]. Growing evidence has demonstrated the pathological morphological and functional properties of the neoangiogenic vessels, such as the disorganized morphology, the lose of basement membrane and pericytes, and the abnormal wall permeability of the microvessels [3-5]. The leaky and unstable intraplaque microvessels serve as a source of intraplaque hemorrhage (IPH) which influences the plaques to develop vulnerable lesions [6, 7]. A remarkable relationship between IPH and subsequent clinical events, including accumulation of lipoproteins, exacerbated inflammation, disintegrated extracellular matrix (ECM), NC expansion, and thinning of the fibrous cap (FC), has been well established in recent decades [8].

In order to analyze the interactions between IPH and other pathophysiological phenomena during atherosclerotic plaque progression, animal models have been developed. In these *in vitro* experiments, IPH can be detected by histological stainings. In clinically, high-resolution MR imaging has been used to detect vulnerable plaque properties such as IPH. However, nowadays the *in vivo* high-resolution imaging technique cannot reveal the microvasculature and the hemodynamics of the microcirculation inside the atherosclerotic plaque. Therefore, the quantitative analysis of intraplaque neovasculature and hemorrhage is unavailable by using the clinical imaging data. Fluid dynamic theoretical and computational models have been successfully

developed and validated for hemodynamics simulation through microvascular networks [9-13]. Based on the two-phase continuum model proposed by Pries et al 1990 [14], mathematical models have been able to take account of large heterogeneities in vascular morphology (i. e., lengths and diameters of microvessels, microvessel density, permeability of microvessel wall) as well as in hemodynamic variables (i. e., hematocrit, blood velocity), which constitute the fundamental characteristics of microcirculation, including intracortical microcirculation [15-17], blood perfusion and oxygen transport in capillaries of skeletal muscle [18] and hemodynamics in angiogenic microvessels of solid tumors [19-21].

In this paper, we perform a series of simulations of angiogenesis in atherosclerotic plaques and hemodynamics in the intraplaque microcirculation. The simulation region and the initial condition settings are based on a histology image of a patient's carotid plaque. The neovasculature is numerically generated based on the angiogenesis modeling developed in our previous work [19]. We assume the neovasculature is generated by the migration and proliferation of endothelial cells (ECs), which are determined by the chemotaxis movement in response to the VEGF gradient and the adherence with ECM. In addition, we perform the hemodynamic calculation by coupling the intravascular blood flow with the transvascular plasma flow and the interstitial fluid flow throughout the surrounding tissues. The IPH is assumed to associate with the diffusional and convective transport of extravascular plasma in the interstitial area. The simulation results are verified by the experimental data and clinical images. The second aim is to investigate the quantitative effects of certain microenvironmental factors on the intraplaque hemorrhage, such as the microvessel density (MVD) and the wall permeability of the neovasculature.

2. Results

Each time step increment ($T=T+1$) corresponds to 150 simulation steps. The simulation of neovascularization ends at $T=13$, when the growing of neovasculature and angiogenic sprouts are both zero. In the following results, the hemodynamics analysis is examined at six stages of angiogenesis during $T=1$ to $T=13$.

2.1 Flow in the angiogenic capillary network

Fig.1 displays the change of P_v with structures of the neovessels at six different stages. The neovasculatures are most numerous in the shoulder area, and growing into the core region gradually. As time passing by and with increased neovessels, intravascular pressure P_v decreases associate with intravascular velocity U_v monotonously from the vasa vasorum of adventitia to the necrotic region. It is found that most reduction of P_v and U_v occur at the first branching of the newvasculature. The mean values of P_v and U_v decrease up to 57% through the whole neovasculature.

2.2 Flow in the interstitial space

Fig.2 shows the dynamic changes of the interstitial fluid pressure P_i inside the atherosclerotic plaque. The increased P_i is observed as early as $T=3$ at the shoulder area. It is noteworthy that the value of P_i and the distribution of high P_i both enlarge with the progression of neovascularization (see Fig. 1). At the late stage of plaque development ($T=13$), the P_i has risen to 2.5mmHg, comparing with the normal interstitial fluid pressure is about zero mmHg. It is noteworthy that the shoulder areas of the plaque are always in a state of interstitial hypertension, which contributes to the intraplaque hemorrhage and plaque vulnerability.

2.3 Intraplaque hemorrhage

The spatial distribution of S_{IPH} is presented in Fig.3. The highlighted areas denote to serious IPH, which are found to be adjacent to the neovasculature. Due to the increasing MVD distributed at the shoulder regions (see Fig.1), the hemorrhage in the same areas is shown to be higher than that inside the necrotic core especially after $T=7$.

However, the high IPH region gradually spreads from the media to the lipid core.

2.4 Comparison of simulation results with MR imaging

We set different thresholds ranging from half of the average pixel values to 2.0 times of that value in increments of 0.1 times, to examine the sensitivity of high IPH areas to the segmentation threshold S_{IPH}^{Thr} .

The optimized threshold S_{IPH}^{Thr} was set to be 1.3 times of the average pixel value to minimize the error with IPH area shown in the MR image. As shown in Fig.4, it can be found that the white areas in the simulation result, corresponding to the dark areas in the MR image, shows the high IPH region mostly distributed in the shoulder areas of the plaque.

2.5 Comparison of simulation results with in vitro data

The growth history curves of MVD and IPH area are presented in Fig. 5A. The MVD of neovasculature increases continually in the simulation with time, which is consistent with the in vitro histological data in rabbits' atherosclerotic plaque [22] (see inserted figure in Fig.5A). The broken line shows a sharp increase of IPH in the late stage coincided with a significant elevated iron area observed in the experiment.

Evidence has showed that the MVD varied in different regions of plaque. MVD in the necrotic core is lower than it in the shoulder and cap regions. The simulation results (white bar) shows the same characteristic with the experimental observation (black bar) [23] in Fig. 5B. However, the MVD values are a bit higher in simulation results than in the experiment, partly due to the cluster of microvessels decrease the MVD counting in the histological examination.

2.6 Sensitivity analysis of IPH to model parameters

In the present model, the factors that directly influence the IPH involved the MVD and the capillary permeability. In order to test the system responses to varied MVD conditions, more simulations are performed with increased and decreased MVD. As shown in Fig.6A, we consider three groups with different MVD (high MVD group, low MVD group and basic MVD group). The fitting curve shows that the IPH area increases with the MVD of the neovasculature. In addition, the change of IPH area caused by MVD tends to be stable when the MVD value was elevated.

The wall permeability of the intraplaque angiogenic microvessel was assumed to be larger than that in the normal capillary. Here, we

reduce the high permeability of capillaries (L_p). As shown in Fig. 6B, we find that the IPH area decreases almost 30% with a low permeability setting of the microvessels. This result suggests that the abnormal function of intraplaque neovasculature could intensify the pathophysiological microenvironment and the IPH area.

3. Discussion

Although the formation and progression of atherosclerotic plaques is understood to be mainly driven by the systemic factors, both in vitro and in vivo observations over the past several decades have established that plaque development involves a complex coordination of systemic and local microenvironmental factors that determine how plaques progress. Uncovering the underlying mechanisms and crosstalk of plaque microenvironment constitutes as prerequisite for the exploration of possibilities targeting the processes within the plaque microenvironment as novel therapeutic strategies. However, there is currently a paucity of data on the dynamic interactions of the plaque microenvironmental components, due to the unavailability of imaging techniques to quantitatively investigate the changes of plaque microenvironment in both animal experiments and clinical settings. In this context, mathematical modeling provides a potential way to assess the dynamics of the plaque microenvironment by describing the spatial-temporal changes of key cells and chemicals according to physical principles and known pathophysiological interactions. To this end, we performed the evolutionary simulations of plaque microenvironmental dynamics. Simulative area was separated into necrotic core, fibrous cap, shoulder and media according to the actual layout of a plaque histology. The neovasculatures are assumed to sprout and proliferate from the adventitial vasa vasorum, and be attracted and interacted with the local chemicals gradient (such as VEGF, ECM and MMPs). These chemical substances are assumed to distribute unevenly in the simulation region as initial conditions, and transport throughout the whole lesion by diffusion and reaction with each other. 2D9P angiogenesis model are carried out to generate the intraplaque neovasculatures. Simulation results demonstrated the process of intraplaque neovascularization for a period of up to 3 weeks. At the late development stages, the structures of neovasculature have shown typical pathophysiological features observed in the experiments, which include high MVD regions distributed at the shoulder regions as well as a low MVD region at the necrotic core. The hemodynamic calculation of neovaculature is performed by considering the fully coupling of the intravascular blood flow with the transvascular plasma flow and the interstitial fluid flow. Based on the simulation results, the extravascular plasma distribution is calculated according to the transvascular plasma flow from the leaky vessel wall and the convective transport within the interstitial tissue, which is used to model the dynamic progression of the IPH area. The hemodynamic results have shown significant consistency with either the histology or the MR images in both quality and quantity ground, including the increased interstitial pressure due to the transvascular plasma flow and the enlarging IPH

extent at the shoulder region of the plaque lesion.

The main objective of this work, to investigate the progression of neovascularization and the changes of hemodynamic microenvironment in the atherosclerotic plaques by using a mathematical modeling system, is successfully achieved. Furthermore, we perform the quantitative analysis of the changes of IPH in response to different microenvironmental factors, including the varied MVD and the permeability of microvessel wall. Simulation results reveal the quantitative relationship between IPH and the varied microenvironmental factors. It is found that the IPH area can be reduced by decreasing the MVD and the permeability. Being comprised of different parameters (such as VEGF) that are easily modified, the present model has the potential to incorporate anti-angiogenic progress. Coupled with drug delivery modeling, we envision that our model and its future advances can serve as a theoretical platform for studying the anti-angiogenic therapy applied on the atherosclerosis.

IPH is demonstrated to be a major factor in the vulnerable plaque development and associated with subsequent clinical events including plaque rupture. However, most of our knowledge about IPH is obtained from the in vitro autopsy studies or animal studies nowadays. This mathematical model would be of great assistance in the set-up of clinical researches by providing a possibility to calculate the IPH dynamics based on patient-specific images. To access the influence of the pre-defined threshold on the comparison of simulation results with MR images, different thresholds are examined to find an appropriate setting for this case. However, more clinical and histological data are needed to validate the functional modules involved in the model.

Nowadays, several imaging modalities are used to characterize one or more plaque microenvironmental factors in vivo. For instance, dynamic contrast-enhanced MRI (DCE-MRI) is proposed to study the intraplaque microvasculature quantitatively and to test the relationship between adventitial perfusion and IPH, while ^{18}F -FDG PET-CT is widely used to evaluate plaque inflammation. Compared with the conventional structural imaging techniques identifying the site and severity of luminal stenosis, these functional assessments may provide more informative values in studying the dynamic microenvironment and consequently to evaluate plaque vulnerability. However, it is unrealistic to carry out multi-modality imaging for every patient due to the technological and socio-economic issues. In this context, this proof-of-concept study aims to present a quantitative evaluation for atherosclerotic plaque microenvironment by using a generalized mathematical modeling system. The power of mathematical modeling lies in its ability to reveal the underlying dynamic mechanism and the physical principles that might have been overlooked in previous

traditional studies. At its best, mathematical modeling provides quantitative supplementary for the imaging data, and enables us to make predictions and early identify which plaque rupture is likely to occur, and leads to a novel and improved ability to assess plaque vulnerability. This will allow actions to be taken in a timely manner to reduce risk of eventual fatal events on an individual basis. Although we have demonstrated the simulation based on MR images in this study, further researches should be addressed by incorporating other available imaging data to expand the application of this mathematical model in clinical assessment.

With the information of plaque microenvironment as initial input, including plaque morphology and composition obtained by imaging technique and biochemical indicators by blood examination, the dynamics and development of the main microenvironmental factors can be calculated by using the developed model system. Based on these results, the evolutional progress of a specific plaque can be predicted. The evaluation indicators of plaque microenvironment include lipid deposition, inflammation, IPH and apoptosis of SMCs. It has been suggested that plaque progression is a modifiable step in the evolution of atherosclerotic plaque. Therefore, a dynamic and quantitative description of plaque microenvironment can provide direct information for personalized treatment to improve the long-term outcomes. We believe the improved evaluation system can help us better understand the interactions among plaque microenvironmental factors and may allow us to predict a possible development of a plaque on an individual basis.

Despite the successful simulations on the dynamic process of intraplaque angiogenesis and IPH and induced changes in plaque microenvironment, some pathophysiological facts are simplified in the model set-up. For example, the progress of plaque growth and evolution is not coupled with the neovascularization. In fact, the hemorrhage into the necrotic core may increase the core size to some extent and result in the luminal narrowing. It will be adapted in the future model by involving the plaque growth in response to the microenvironment caused by the intraplaque neovascularization and IPH. Due to the lack of experimental data, some parameters are estimated in the model, such as the permeability of neovessels. More realistic adjustments will improve the model accuracy. Development of 2D model to 3D model may provide more directions and spaces for intraplaque neovascularization and IPH, which should be addressed in the future work.

4. Conclusions

A mathematical modelling system was established by incorporating intraplaque angiogenesis and hemodynamic calculation of the microcirculation, in order to obtain the quantitative evaluation of the influences of intraplaque neovascularization and hemorrhage on the carotid plaque progression. The simulations of the model not only reproduced a series of pathophysiological phenomena during the plaque development, including the high microvessel density region at the shoulder areas, the enlarged necrotic core, and the intraplaque hemorrhage, but also revealed the quantitative relationship between intraplaque hemorrhage and the varied microenvironmental factors. The simulational results demonstrated that the IPH area can be reduced by decreasing the MVD and the permeability of the neovasculature. The current quantitative model could help us to better understand the roles of microvascular and intraplaque hemorrhage during the carotid plaque progression. Additionally, with more patient-specific data, the model could be improved to predict the possible development of an individual plaque based on the dynamic interactions of the plaque microenvironmental factors.

5. Methods

5.1 Setup of angiogenic microvasculature

A male patient, 76 years old, had an 80% left carotid stenosis. MR imaging study of the carotid plaque was performed using our established protocol [24]. Carotid endarterectomy was performed following the MR imaging study and histological analysis was performed. The histology data with the hematoxylin and eosin (HE) -stained was used to define the region of the model, which is a two-dimensional region of 4mm×4mm, discreted into 200×200 grids uniformly. We divided the plaque into three different areas: necrotic core (NC), shoulders (SA) and fibrous cap (FC) (Fig.7) [25]. We first processed the image and outlined the boundary of the plaque area (black line shown in supplemental Fig.7A). Then we connected the two tips of plaque with the center of the lumen, resulting in an angle alpha (Fig.7B). The point where the bisector of alpha cut the boundary of plaque was called b. The two tips of plaque were connected with b and their extension lines were used to distinguish the shoulders with the necrotic core. The narrow area between the lumen and the plaque was defined to be fibrous cap. Twelve sprouts (red dots shown in Fig.7B) from vasa vasorum were assumed to be located on the media, uniformly with 30 degree steps as the initial condition of intraplaque neovascularization.

By considering four diagonal directions based on the classic two-dimensional five-point (2D5P) modeling of neovascularization proposed by Anderson & Chaplain (1998) [26], two-dimensional nine-point (2D9P) model was introduced in our previous published study for solid tumor angiogenesis [19]. In this work, 2D9P model was adopted to describe the neovascularization of intraplaque angiogenic microvessels. The current model focused on six key components involved in the intraplaque angiogenesis, i.e., the ECs density (n), the smooth muscle cells (SMCs) (s), the macrophages (g), VEGF concentration (c), ECM concentration (f), and matrix metalloproteinase (MMPs) concentration (m). The chemical substances were assumed to change with spatial and time, and satisfied the following coupled reaction-diffusion equations:

$$\frac{\partial n}{\partial t} = D_n \nabla^2 n - \nabla \cdot \left(\frac{\chi_0 k_1}{k_1 + c} n \nabla c \right) - \nabla \cdot (\rho_0 n \nabla f) \quad (1)$$

$$\frac{\partial c}{\partial t} = D_c \nabla^2 c - \lambda n c + \eta_c s c \quad (2)$$

$$\frac{\partial f}{\partial t} = -\eta_f m f \quad (3)$$

$$\frac{\partial m}{\partial t} = D_m \nabla^2 m + \kappa_m n + \kappa_g g - \sigma_m m \quad (4)$$

The 2D9P hybrid discrete-continuum angiogenesis model assumed the migration of the ECs through random motility, the chemotaxis in response to the VEGF attraction and the haptotaxis in response to the ECM adherence (Eq. (1)). The changes of chemicals satisfied the reaction-diffusion equations (Eqs. (2)-(4)). Specifically, the VEGF was assumed to diffuse, be produced by SMCs and consumed by ECs, with the diffusion coefficient D_c and constant parameters η_c and λ respectively.

The ECM was degraded by MMPs linearly with coefficient η_f . The MMPs was diffused, be produced by ECs and macrophages, as well as decay by itself, with the diffusion coefficient D_m and constant parameters $\kappa_m, \kappa_g, \sigma_m$, respectively.

The initial conditions of the three chemicals in Eqs. (2)-(4) were:

$$c(x, y, 0) = \frac{(v - r_1)^2}{v - 0.4771} + \frac{(v - r_2)^2}{v - 0.4771} \quad (5)$$

$$f(x, y, 0) = 1 \quad (6)$$

$$m(x, y, 0) = 0 \quad (7)$$

The VEGF was assumed to be high concentration in the shoulder areas. v was a positive constant and r_1, r_2 were the distances to the center points of the two shoulders (area SA in Fig. 7), respectively.

$$n(x, y, 0) = \begin{cases} 1, & \text{Sprouts} \\ 0, & \text{else} \end{cases} \quad (8)$$

$$s(x, y, 0) = \begin{cases} 0, & \text{NC and Lumen} \\ 1, & \text{else} \end{cases} \quad (9)$$

$$g(x, y, 0) = \begin{cases} 1, & \text{shoulder} \\ 0, & \text{else} \end{cases} \quad (10)$$

5.2 Hemodynamic calculation in microcirculation

There were three parts in the hemodynamic calculation of neovasculatures, i. e., the intravascular blood flow, the interstitial fluid flow and the transvascular flow (Fig. 8) [27].

Blood flow within point C from its adjacent points (if there was a vessel segment, which represented by a binary matrix $B_{(c)}^k$) satisfied

the flow conservation equation:

$$\sum_{k=1}^8 Q_{(c)}^k B_{(c)}^k = 0 \quad (11)$$

$$Q_{(c)}^k = Q_{V,(c)}^k - Q_{I,(c)}^k \quad (12)$$

where $Q_{I,(c)}^k$ was the transvascular plasma flow (see Eq. (16)) and $Q_{V,(c)}^k$ represented intravascular blood flow without transvascular transport, and followed the Poiseuille' s law

$$Q_{V,(c)}^k = \frac{\pi \bar{R}_k^4 (\Delta P_{V,(c)})}{8 \bar{\mu}_k \Delta l_k} \quad (13)$$

The interstitial flow rate \bar{U}_i satisfied the continuity equation as well as the Darcy' s law [28, 29]:

$$\nabla \cdot \bar{U}_i = \sum Q_{I,(c)}^k \quad (14)$$

$$\bar{U}_i = -K \nabla P_i \quad (15)$$

where K denoted the hydraulic conductivity coefficient of the interstitial tissue. The transvascular flow $Q_{I,(c)}^k$ was governed by the Starling' s law:

$$Q_{I,(c)}^k = 2\pi \bar{R}_k \Delta l_k \cdot L_p (\bar{P}_{V,(c)}^k - \bar{P}_{i,(c)}^k - \sigma_T (\pi_V - \pi_i)) \quad (16)$$

$\bar{P}_{V,(c)}^k$ and $\bar{P}_{i,(c)}^k$ represented the average pressure and the average interstitial pressure in and outside the vessel segment k, respectively. σ_T was the average osmotic reflection coefficient for plasma; π_V, π_i were the colloid osmotic pressure of blood plasma and interstitial fluid respectively.

S_{IPH} represented the extravascular plasma concentration, which was governed by the extravascular plasma transport throughout the interstitial tissue and the transvascular plasma flow across the leaky wall of the angiogenic microvessels.

$$\frac{\partial S_{IPH}}{\partial t} = \varphi \cdot \nabla^2 S_{IPH} - \Psi S_{IPH} \cdot U_i + \gamma Q_t \quad (17)$$

To compared the simulation results of IPH with MR images, where $S_{IPH} > S_{IPH}^{Thr}$, we considered it as high IPH regions. S_{IPH}^{Thr} was a threshold determined by the MR images. The baseline parameter values were listed in Table 1.

Table 1 The baseline parameter values of the simulation.

Parameter	Baseline value	Parameter	Baseline value
D_n (10^{-10} cm ² /s)	1	χ_0 (cm ² /s·M)	2600
k_i (10^{-10} M)	7	ρ_0 (cm ² /s·M)	1000
D_c (10^{-7} cm ² /s)	2.9	λ (M ⁻¹ ·s ⁻¹)	750
η_c (M ⁻¹ ·s ⁻¹)	750	n_f (cm ³ /s·M)	130
D_m (10^{-10} cm ² /s)	1	κ_m (10^{-3} cm ⁻³ ·s ⁻¹)	1
κ_g (10^{-3} cm ⁻³ ·s ⁻¹)	1	σ_m (10^{-8} s ⁻¹)	1
v	1.07	R_o (μ m)	4 [31]
K (10^9 cm ² /mmHg·s)	41.3 [30]	L_p (10^{-7} cm/mmHg·s)	2.8 [30]
σ_T	0.82 [30]	π_V (mmHg)	20 [30]
π_i (mmHg)	15 [30]	φ	0.4
ψ	0.05	γ	0.4
β	0.4	P_{in} (mmHg)	10
P_{out} (mmHg)	1		

5.3 Principles of 2D9P angiogenesis model

We used the Euler's nine point finite difference scheme to discretize the above equations [19, 26], in which the discretized equation of ECs was:

$$n_{i,j}^{q+1} = n_{i,j}^q P_0 + n_{i+1,j}^q P_1 + n_{i-1,j}^q P_2 + n_{i,j+1}^q P_3 + n_{i,j-1}^q P_4 \\ + n_{i-1,j+1}^q P_5 + n_{i+1,j-1}^q P_6 + n_{i-1,j-1}^q P_7 + n_{i+1,j+1}^q P_8$$

(18)

where the subscripts i , j and the superscripts q specified the location on the grid and the time steps, respectively. The 2D9P model assumed that the coefficients $P_0 \sim P_8$ were the probability density function to determine the movement direction of the sprouts. The nine coefficients corresponded to the nine possible movements for ECs, including stationary, four horizontal and vertical directions, and four diagonal directions (shown in the Fig.8). In each time step, the probability density functions $P_0 \sim P_8$ were integrated into the cumulative distribution function. The probability of the EC to migrate to the certain neighbor grid was set to be proportional to the value of the cumulative distribution function. After the ECs distribution updated, there were two 2D binary matrixes A and B to record the topology of the vessel network. The former was imposed on the simulation grids, while the latter on the vessel segments. The values of both were 1 if the EC/vessel was on the grid/segment, and 0 if it is not.

The new sprouts were assumed to generate only from the existing sprout tips, and the newly formed sprouts were unlikely to branch immediately. Sufficient space locally was requisite for the forming of a new sprout. Furthermore, we assumed that the probability of

generating a new sprout was dependent on the local concentration of VEGF. If one sprout tip encountered another sprout or vessels, anastomosis would occur. As a result of the tip-to-tip fusions, only one of the original sprouts continued to grow.

5.4 Simulation algorithms

The simulation algorithms of hemodynamics throughout the neovasculature were as follows:

a) Set initial pressure P_{in} of 12 entrances and exits where vessels stop growing with pressure P_{out} . The initial iteration value is also set.

b) Solved intravascular pressure P_V and its relative error.

In the model, we used iterative method to solve the pressure $P_{V,(c)}$:

$$P_{V,(c)}^{m+1} = \frac{\sum_{k=1}^8 \left\{ \left[\frac{\bar{R}_k^4}{\bar{\mu}_k \Delta l_k} - 8\bar{R}_k \Delta l_k L_p \right] P_{V,(k)}^m + 16\bar{R}_k \Delta l_k L_p [\bar{P}_{i,(c)}^k + \sigma_T(\pi_V - \pi_i)] \right\} \cdot B_{(c)}^k}{\sum_{k=1}^8 \left(\frac{\bar{R}_k^4}{\bar{\mu}_k \Delta l_k} + 8\bar{R}_k \Delta l_k L_p \right) \cdot B_{(c)}^k} \quad (19)$$

$$errP_V = \sum |P_{V,(j,k)} - P_{V,(j,k)}^o| / \sum P_{V,(j,k)} \quad (20)$$

c) Calculated interstitial pressure P_i and its relative error.

Using FTCS discrete equation of (14)–(16):

$$\frac{P_{i,(j+1,k)}^m - 2P_{i,(j,k)}^m + P_{i,(j-1,k)}^m}{\Delta x^2} + \frac{P_{i,(j,k+1)}^m - 2P_{i,(j,k)}^m + P_{i,(j,k-1)}^m}{\Delta y^2} = \alpha^2 (P_{i,(j,k)}^{m+1} - P_{e,(j,k)}) A_{j,k} \quad (21)$$

In the model, the successive over relaxation (SOR) iteration method was used to solve the formula, ω was the coefficient of relaxation:

$$P_{i,(j,k)}^{m+1} = P_{i,(j,k)}^m + \frac{\omega}{4 + \Delta x^2 \alpha^2 A_{j,k}} [\Delta x^2 \alpha^2 A_{j,k} P_{e,(j,k)} + P_{i,(j+1,k)}^m + P_{i,(j-1,k)}^m + P_{i,(j,k+1)}^m + P_{i,(j,k-1)}^m - (4 + \Delta x^2 \alpha^2 A_{j,k}) P_{i,(j,k)}^m] \quad (22)$$

$$errP_i = \sum |P_{i,(j,k)} - P_{i,(j,k)}^o| / \sum P_{i,(j,k)} \quad (23)$$

where P_e was the effective pressure of capillary and equaled to

$$P_e = P_V - \sigma_T(\pi_V - \pi_i)$$

d) Estimated the maximal iterative error, repeat b) to c) until $errP_V \leq 10^{-6}$ and $errP_i \leq 10^{-6}$.

e) Calculated the intravascular flow Q_v , and the transvascular flow Q_t using Eqs. (13), (16).

- f) Calculated the interstitial fluid velocity U_i using Eqs. (14), (15)
- g) Calculated intraplaque hemorrhage area matrix S_{IPH} (Eq. (17)).

Declarations

- Ethics approval and consent to participate

Not applicable

- Consent for publication

Not applicable

- Availability of data and materials

The datasets used and/or analysed during the current study are available from the corresponding author on reasonable request.

- Competing interests

The authors declare that they have no competing interests.

- Funding

This research is supported by the National Nature Science Foundation of China (Grant numbers 11972118, 61821002, 11772093, 11972117, 12072074), the Fundamental Research Funds for the Central Universities, the National Demonstration Center for Experimental

Biomedical Engineering Education (Southeast University, Nanjing, China), the Funds for Young Zhishan Scholars (Southeast University, Nanjing, China), and ARC (Grant number FT140101152, DP200103492).

- Authors' contributions

YC designed the whole study. JP analyzed the patient data. YC and JP performed the program. ZL organized the simulation results. YC was a major contributor in writing the manuscript. All authors read and approved the final manuscript.

- Acknowledgements

Not applicable

References

1. Grønholdt, M.L., et al. (1998). Coronary atherosclerosis: determinants of plaque rupture. *European Heart Journal*, 19 suppl c, C24-C29.
2. Silvestre-Roig, C., et al. (2014). Atherosclerotic plaque destabilization: mechanisms, models, and therapeutic strategies. *Circulation Research*, 114(1), 214-226.
3. Fok, P.W. (2012). Growth of necrotic cores in atherosclerotic plaque. *Mathematical Medicine and Biology*, 29(4), 301-327.
4. Hansson, G.K., et al. (2015). Inflammation and plaque vulnerability. *Journal of Internal Medicine*, 278(5), 483-493.
5. Kavurma, M.M., et al. (2017). The walking dead: macrophage inflammation and death in atherosclerosis. *Current Opinion in Lipidology*, 28(2), 91-98.
6. Kurata, M., et al. (2014). Microvasculature of carotid atheromatous plaques: hemorrhagic plaques have dense microvessels with fenestrations to the arterial lumen. *Journal of Stroke and Cerebrovascular Diseases*, 23(6), 1440-1446.
7. Camare, C., et al. (2017). Angiogenesis in the atherosclerotic plaque. *Redox Biology*, 12, 18-34.
8. Michel, J.-B., et al. (2014). Pathology of human plaque vulnerability: Mechanisms and consequences of intraplaque haemorrhages. *Atherosclerosis*, 234(2), 311-319.
9. Li, Z.Y., et al. (2006). How Critical Is Fibrous Cap Thickness to Carotid Plaque Stability? A Flow-Plaque Interaction Model. *Stroke-A Journal of Cerebral Circulation*, 37(5), 1195.
10. Lu, J., et al. (2015). Finite element analysis of mechanics of neovessels with intraplaque hemorrhage in carotid atherosclerosis. *BioMedical Engineering OnLine*, 14 Suppl 1, S3.
11. Hao, W. and A. Friedman. (2014). The LDL-HDL profile determines the risk of atherosclerosis: a mathematical model. *PLoS One*, 9(3), e90497.
12. El Khatib, N., et al. (2012). Reaction-diffusion model of atherosclerosis development. *Journal of Mathematical Biology*, 65(2), 349-374.
13. Hidalgo, A., et al. (2013). Numerical and analytical study of an atherosclerosis inflammatory disease model. *Journal of Mathematical Biology*, 68(7), 1785-1814.
14. Pries, A.R., et al. (1990). Blood flow in microvascular networks. Experiments and simulation. *Circulation Research*, 67(4), 826-834.
15. Godde, R. and H. Kurz. (2001). Structural and biophysical simulation of angiogenesis and vascular remodeling. *Developmental Dynamics*, 220(4), 387-401.
16. Lorthois, S. and F. Cassot. (2010). Fractal analysis of vascular networks: insights from morphogenesis. *Journal of Theoretical Biology*, 262(4), 614-633.
17. Mantzaris, N.V., et al. (2004). Mathematical modeling of tumor-induced angiogenesis. *Journal of Mathematical Biology*, 49(2), 111-187.
18. Heuslein, J.L., et al. (2015). Computational Network Model Prediction of Hemodynamic Alterations Due to Arteriolar Rarefaction and Estimation of Skeletal Muscle Perfusion in Peripheral Arterial Disease. *Microcirculation*, 22(5), 360-369.
19. Cai, Y., et al. (2016). Mathematical Modelling of a Brain Tumour Initiation and Early Development: A Coupled Model of Glioblastoma Growth, Pre-Existing Vessel Co-Option, Angiogenesis and Blood Perfusion. *PLoS One*, 11(3), e0150296.
20. Cai, Y., et al. (2011). Coupled modelling of tumour angiogenesis, tumour growth and blood perfusion. *Journal of Theoretical Biology*, 279(1), 90-101.

21. Naghavi, N., et al. (2016). Simulation of tumor induced angiogenesis using an analytical adaptive modeling including dynamic sprouting and blood flow modeling. *Microvascular Research*, 107, 51-64.
22. Kockx, M.M., Cromheeke, K.M., Knaapen, M.W., Bosmans, J.M., De Meyer, G.R., Herman, A.G., Bult, H. (2003). Phagocytosis and macrophage activation associated with hemorrhagic microvessels in human atherosclerosis. *Arteriosclerosis, Thrombosis, and Vascular Biology* 23, 440-446.
23. Kurata, M., Nose, M., Shimazu, Y., Aoba, T., Kohada, Y., Yorioka, S., Suehiro, S., Fukuoka, E., Matsumoto, S., Watanabe, H., Kumon, Y., Okura, T., Higaki, J., Masumoto, J. (2014). Microvasculature of Carotid Atheromatous Plaques: Hemorrhagic Plaques Have Dense Microvessels with Fenestrations to the Arterial Lumen. *Journal of Stroke and Cerebrovascular Diseases* 23, 1440-1446.
24. Li, Z.Y., Zhu, C., Teng, Z., Gillard, J.H. (2010). Stress Analysis of Carotid Plaque Based on in Vivo MRI of Acute Symptomatic and Asymptomatic Patients. *Springer Berlin Heidelberg* 31, 891-894.
25. Ionita, M.G., van den Borne, P., Catanzariti, L.M., Moll, F.L., de Vries, J.P., Pasterkamp, G., Vink, A., de Kleijn, D.P. (2010). High neutrophil numbers in human carotid atherosclerotic plaques are associated with characteristics of rupture-prone lesions. *Arteriosclerosis, Thrombosis, and Vascular Biology* 30, 1842-1848.
26. Anderson, A.R.A. and M.A.J. Chaplain. (1998). Continuous and discrete mathematical models of tumor-induced angiogenesis. *Bulletin of Mathematical Biology*, 60(5), 857-899.
27. Guo M, Cai Y, Yao X, Li Z. (2018). Mathematical modeling of atherosclerotic plaque destabilization: Role of neovascularization and intraplaque hemorrhage. *J Theor Biol.* 450, 53 - 65.
28. Guo M, Cai Y, He C, Li Z. (2019). Coupled Modeling of Lipid Deposition, Inflammatory Response and Intraplaque Angiogenesis in Atherosclerotic Plaque. *Ann Biomed Eng.* 47, 439 - 452.
29. Wu, J., et al. (2009). Study of tumor blood perfusion and its variation due to vascular normalization by anti-angiogenic therapy based on 3D angiogenic microvasculature. *Journal of Biomechanics*, 42(6), 712-721.
30. Rademakers, T., et al. (2013). Plaque-associated vasa vasorum in aged apolipoprotein E-deficient mice exhibit proatherogenic functional features in vivo. *Arteriosclerosis Thrombosis and Vascular Biology*, 33(2), 249-256.
31. Phinikaridou, A., et al. (2016). Increased Vascular Permeability Measured With an Albumin-Binding Magnetic Resonance Contrast Agent Is a Surrogate Marker of Rupture-Prone Atherosclerotic Plaque. *Circulation-Cardiovascular Imaging*, 9(12), e004910.

Figure legends

Figure 1. Spatial distribution of the intravascular pressure P_v in the induced capillary network at six different stages.

Figure 2. Spatial distribution of the interstitial fluid pressure P_i at six different stages.

Figure 3. Phenomena of intraplaque hemorrhage at six different stages.

Figure 4. Simulated results of intraplaque hemorrhage (A) and MR image of plaque (B). The white areas in (A), corresponding to the dark areas in (B), shows the IPH region mostly distributed in the shoulder areas of the plaque.

Figure 5. Comparison of simulation results with in vitro data. (A) The growth history curves of MVD and IPH area; (B) MVD in different regions of plaque.

Figure 6. Sensitivity analysis of IPH to model parameters. (A) Investigation of the influence of varied MVD on the IPH area; (B) Influence of the permeability of the angiogenic vessel wall to IPH area.

Figure 7. (A) Histology of a patient's plaque; (B) Schematics of the segmentation of simulation region. The plaque was divided into three different areas: necrotic core (NC), shoulders (SA) and fibrous cap (FC).

Figure 8. Schematics of the 2D9P angiogenesis model and the blood flow through one segment.

Figures

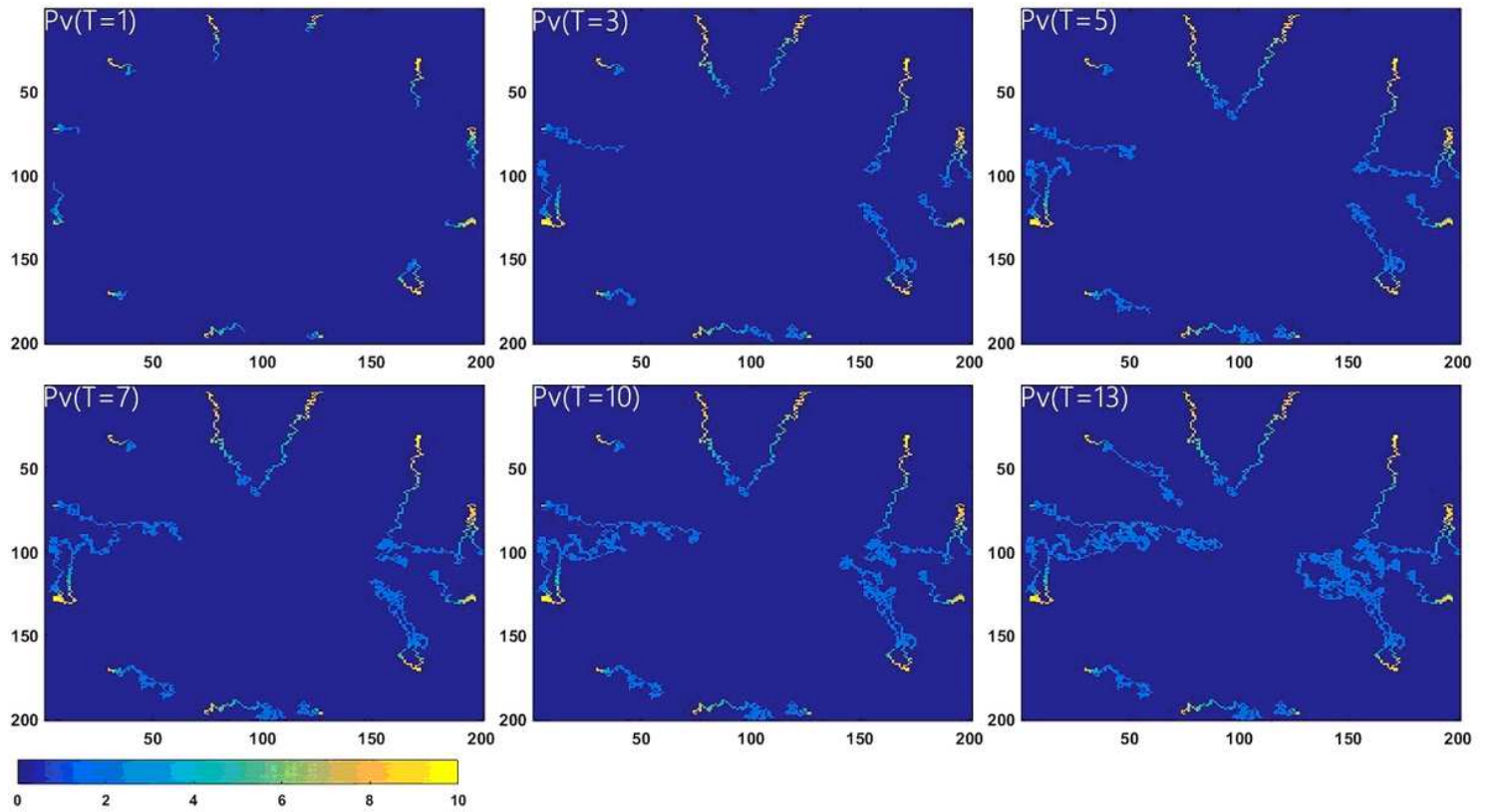


Figure 1

Spatial distribution of the intravascular pressure P_v in the induced capillary network at six different stages.

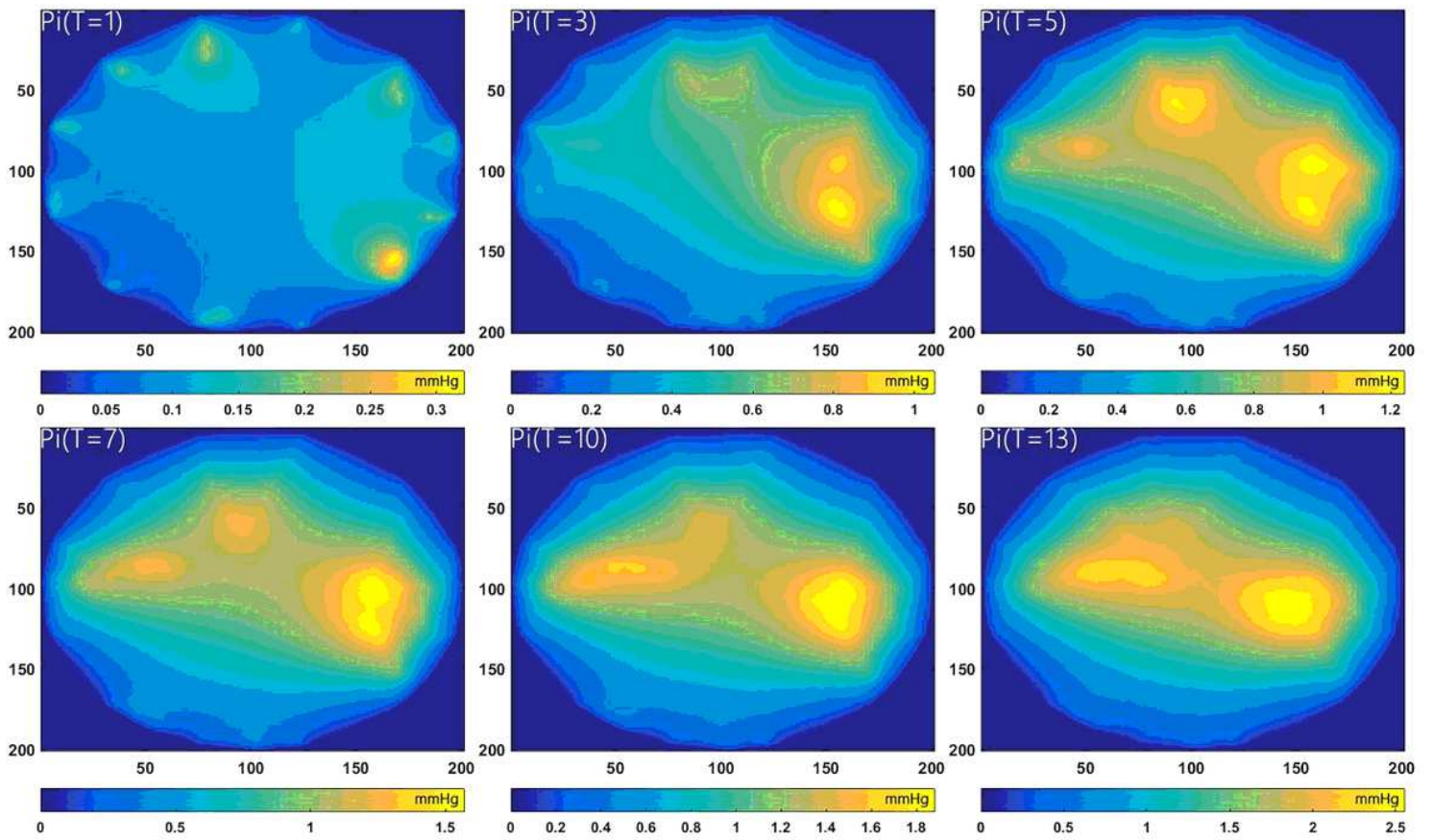


Figure 2

Spatial distribution of the interstitial fluid pressure P_i at six different stages.

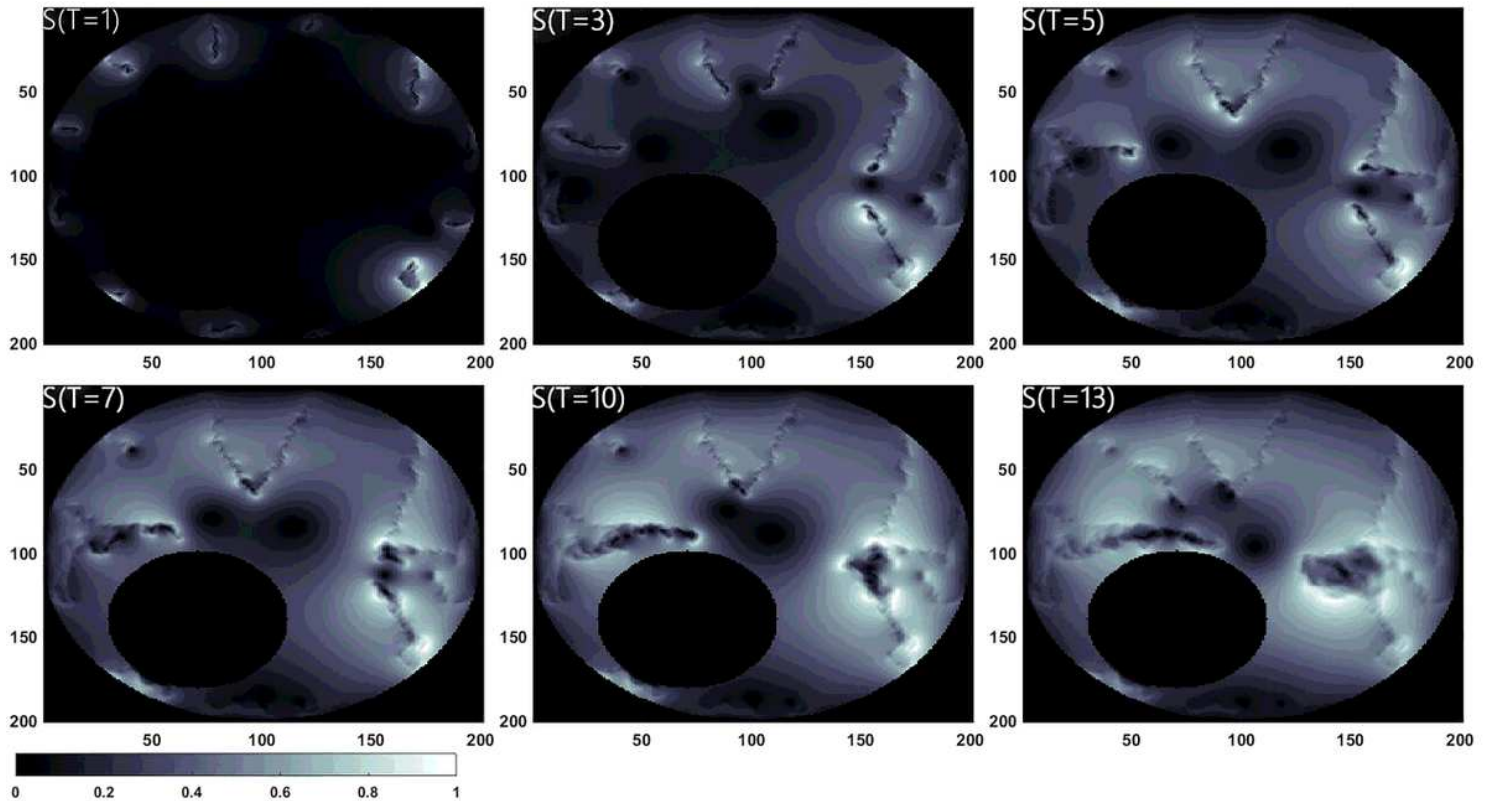


Figure 3

Phenomena of intraplaque hemorrhage at six different stages.

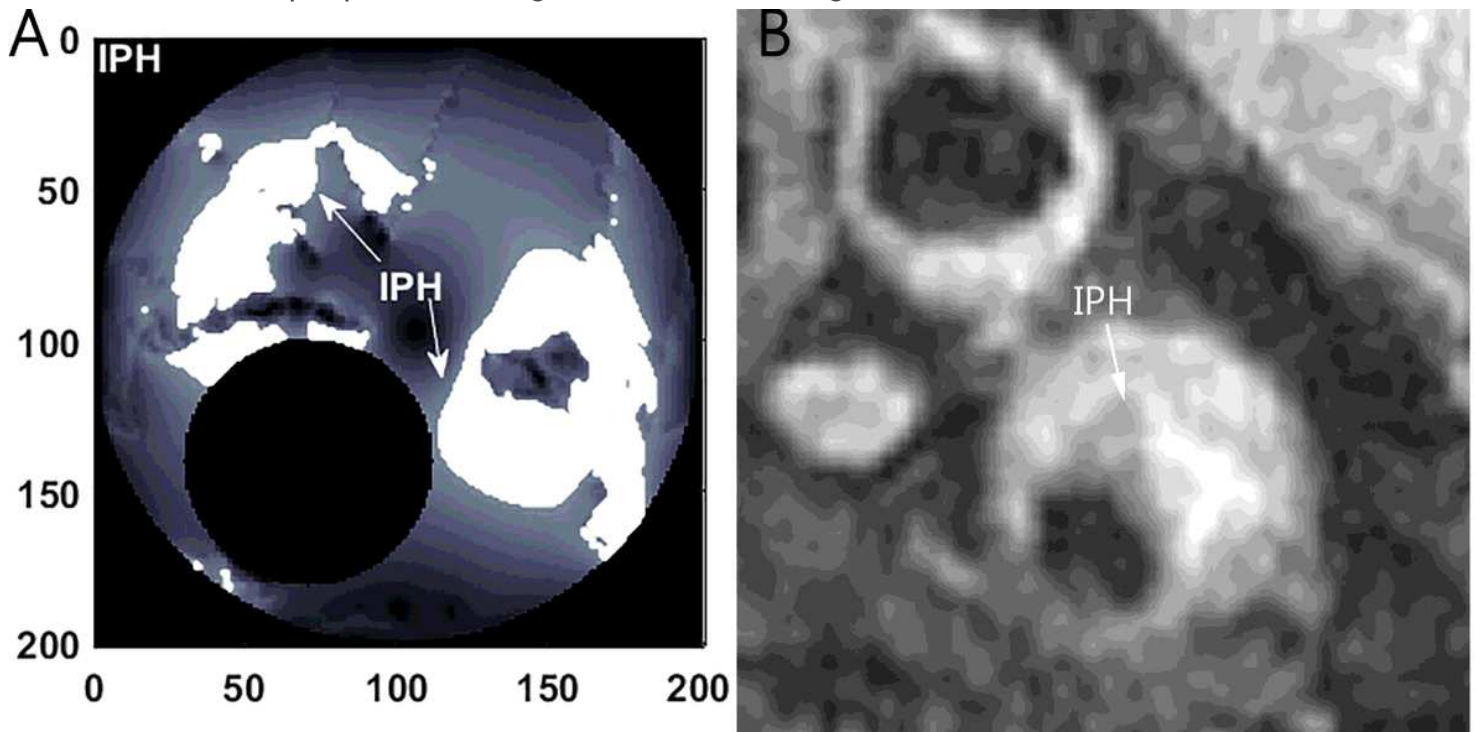


Figure 4

Simulated results of intraplaque hemorrhage (A) and MR image of plaque (B). The white areas in (A), corresponding to the dark areas in (B), shows the IPH region mostly distributed in the shoulder areas of the plaque.

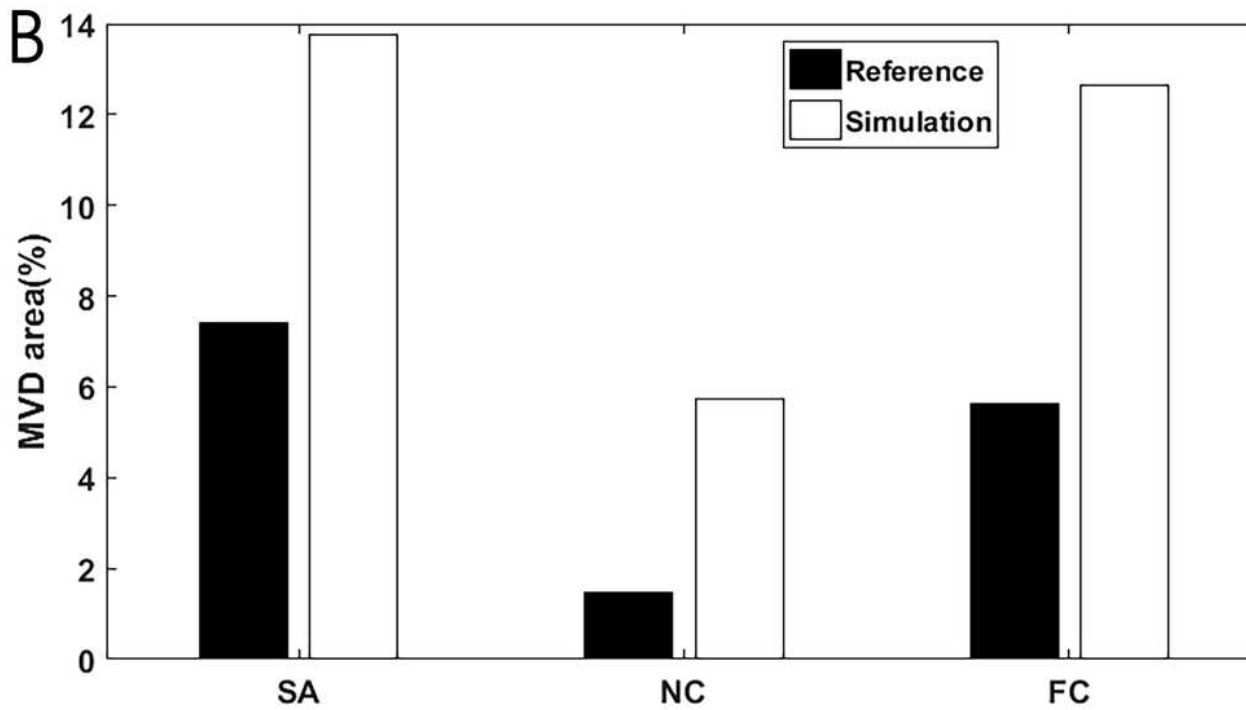
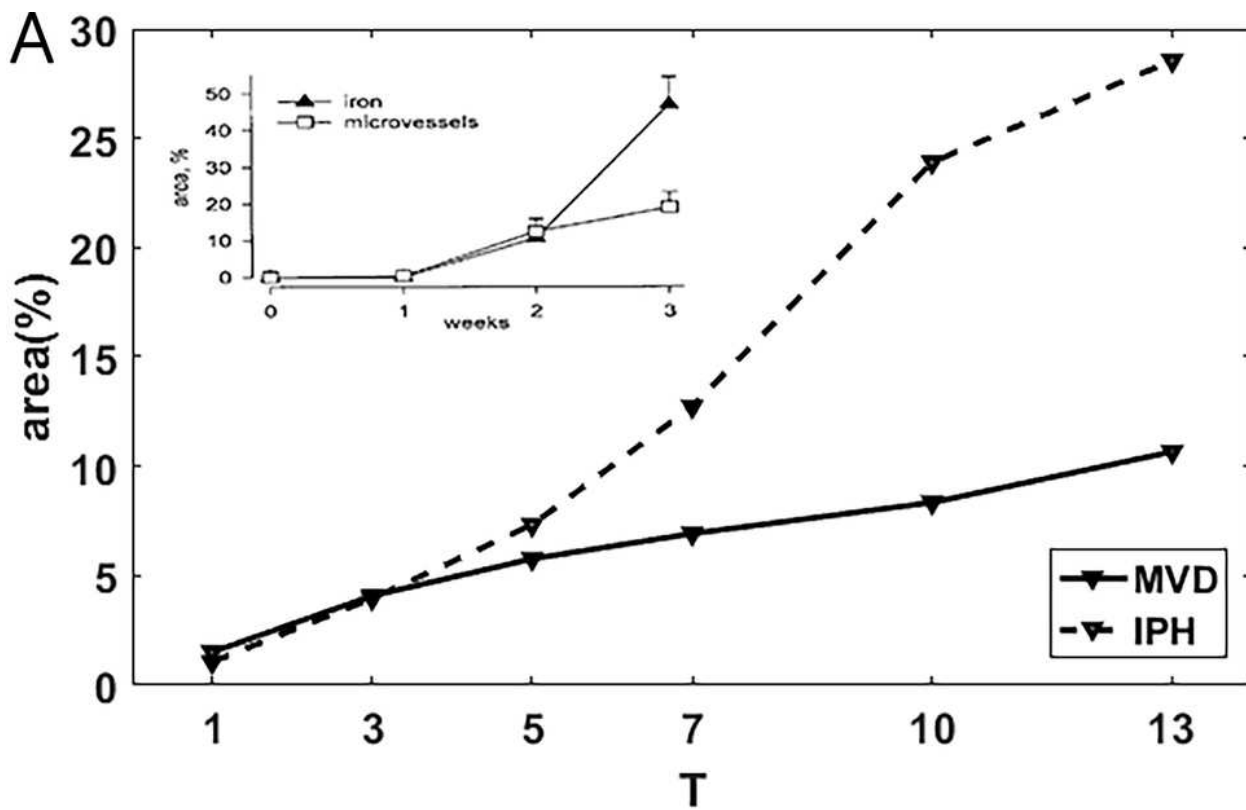


Figure 5

Comparison of simulation results with in vitro data. (A) The growth history curves of MVD and IPH area; (B) MVD in different regions of plaque.

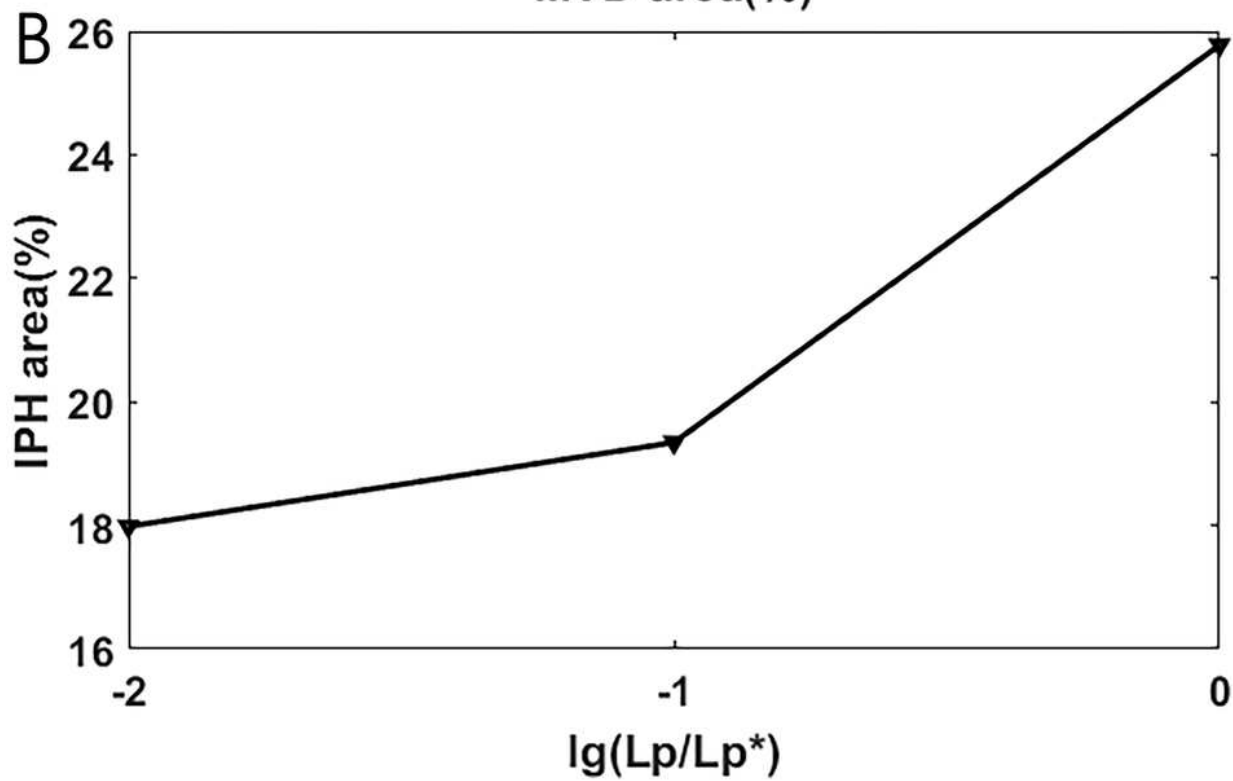
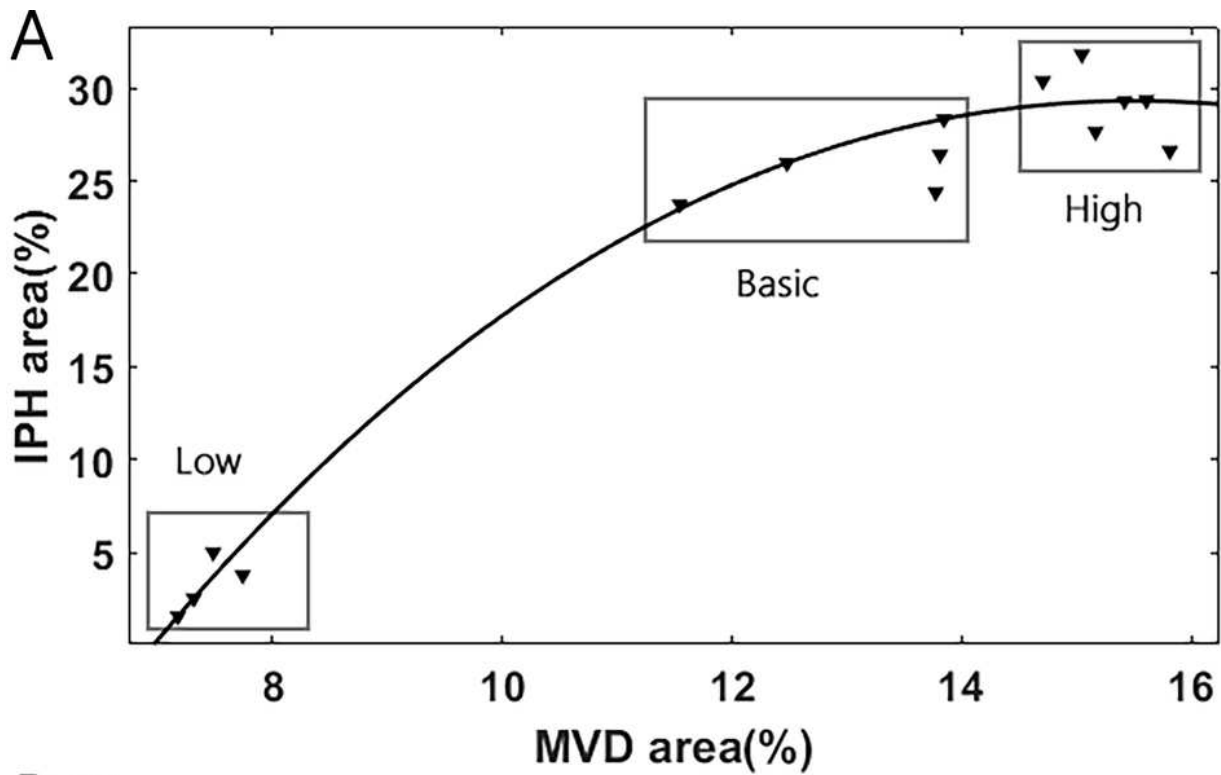


Figure 6

Sensitivity analysis of IPH to model parameters. (A) Investigation of the influence of varied MVD on the IPH area; (B) Influence of the permeability of the angiogenic vessel wall to IPH area.

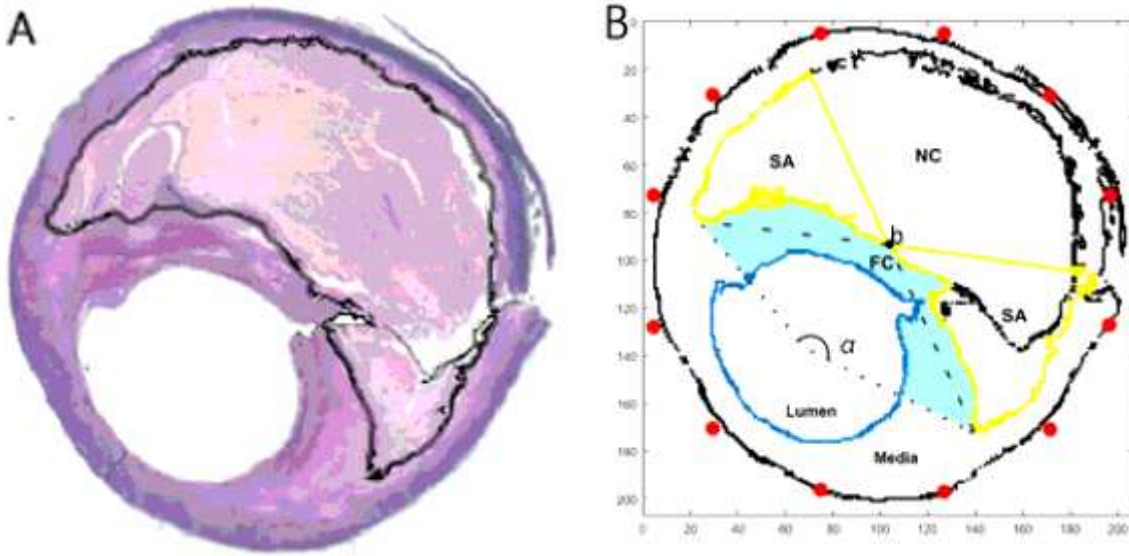


Figure 7

(A) Histology of a patient's plaque; (B) Schematics of the segmentation of simulation region. The plaque was divided into three different areas: necrotic core (NC), shoulders (SA) and fibrous cap (FC).

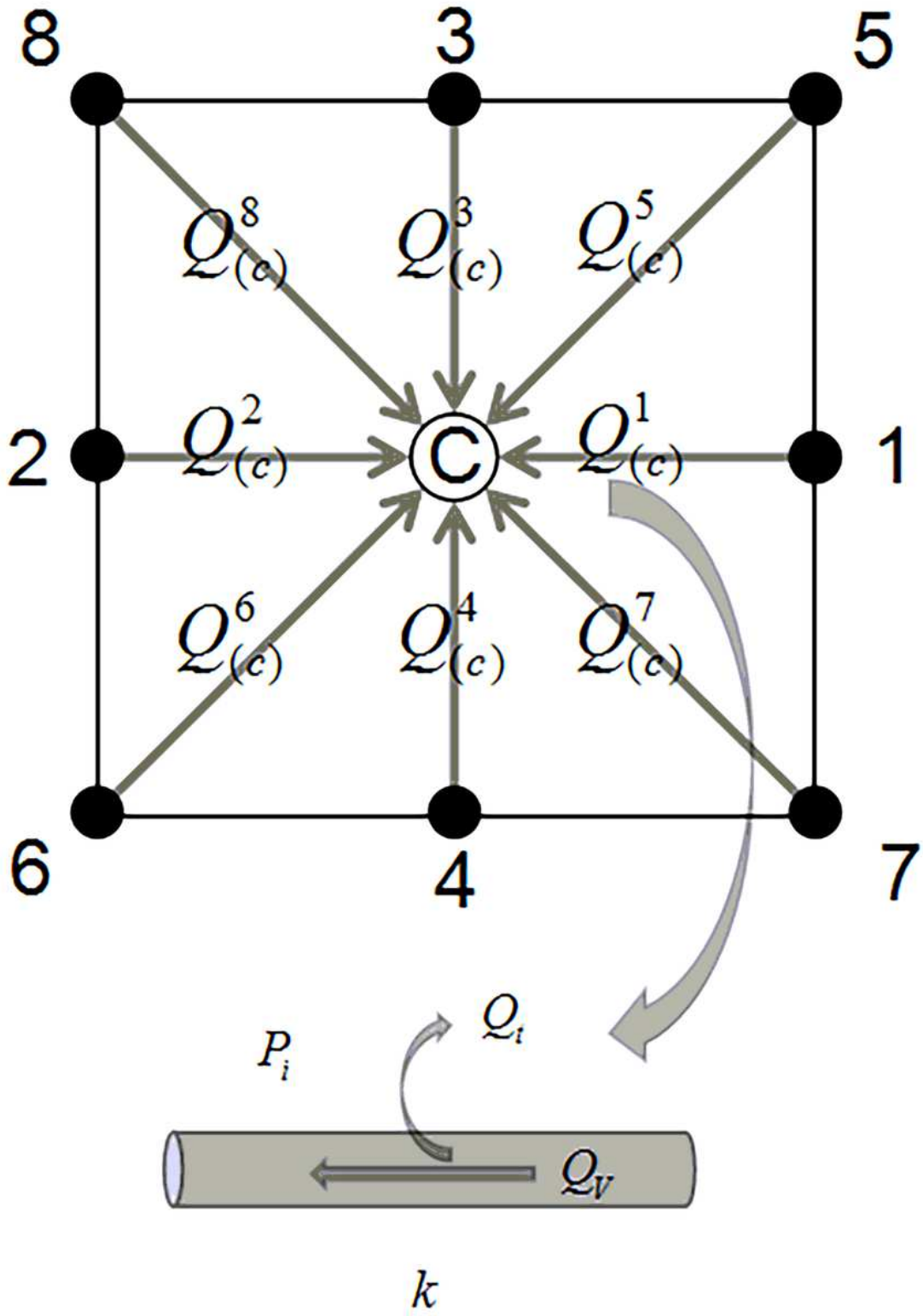


Figure 8

Schematics of the 2D9P angiogenesis model and the blood flow through one segment.